RSC Advances

PAPER

View Article Online
View Journal | View Issue

Cite this: *RSC Adv.*, 2019, **9**, 41886

Nanoporous hybrid CuO/ZnO/carbon papers used as ultrasensitive non-enzymatic electrochemical sensors†

Minwei Zhang, *[ab] Wenrui Zhang,[a] Fei Chen,[a] Chengyi Hou, [bc] Arnab Halder [b] and Qijin Chi *[b]

In this research, we demonstrate a facile approach for the synthesis of a graphite-analogous layer-by-layer heterostructured CuO/ZnO/carbon paper using a graphene oxide paper as a sacrificial template. Cu^{2+} and Zn^{2+} were inserted into the interlayer of graphene oxide papers *via* physical absorption and electrostatic effects and then, the M^{n+}-graphene oxide paper was annealed in air to generate 2D nanoporous CuO/ZnO nanosheets. Due to the graphene oxide template, the structure of the obtained CuO/ZnO nanosheets with an average size of ~50 nm was duplicated from the graphene oxide paper, which displayed a layer-by-layer structure on the microscale. The papers composed of nanosheets had an average pore size of ~10 nm. Moreover, the as-prepared CuO–ZnO papers displayed high hybridization on the nanoscale. More importantly, the thickness of the single-layer CuO/ZnO nanosheet was about 2 nm (3–4 layer atom thickness). The as-synthesized nano-hybrid material with a high specific surface area and conjunct bimodal pores could play key roles for providing a shorter diffusion path and rapid electrolyte transport, which could further facilitate electrochemical reactions by providing more active sites. As an electrode material, it displayed high performances as a non-enzymatic sensor for the detection of glucose with a low potential (0.3 V *vs.* SCE), high sensitivity (3.85 mA mM^{-1} cm^{-2}), wide linear range (5 μM to 3.325 mM), and low detection limit of 0.5 μM.

Received 9th October 2019
Accepted 3rd December 2019

DOI: 10.1039/c9ra08223a

rsc.li/rsc-advances

CuO/ZnO-based multifunctional nanohybrid materials are widely used in various applications, such as sensors,[1–5] photo degradation,[6,7] catalysis,[8] energy storage,[9] memory applications,[10] and especially non-enzymatic sensors for the detection of glucose.[13,14] The heterostructured ZnO–CuO composite material has been extensively used for non-enzymatic sensing applications due to the extension of its electron depletion layer through the formation of a p–n junction.[11,12] Therefore, a number of studies have been devoted to the synthesis of CuO–ZnO hybrid materials,[12–18] such as three-dimensional porous ZnO–CuO hierarchical nanocomposites fabricated by coelectrospinning[19] and flower-like CuO–ZnO heterostructured nanowire arrays on a mesh substrate obtained using a solution method.[20] Among them, 0D nanoparticles or 1D nanowires have been dominant for a long period. Recently, ultrathin two-dimensional (2D) nanostructured materials have attracted increasing attention due to their large surface-to-volume ratios and confined thickness on the nanometer scale and tunable nanoporous structure. They are expected to exhibit high performances for achieving superior catalytic, photovoltaic and electrochemical applications. Thus, 2D metal oxide (MO) nanostructures have been widely demonstrated in adsorption, catalysis, energy conversion and storage, and optoelectronic and biological applications.[21] However, it is still very challenging to prepare large-scale 2D ultrathin and porous structured nanofilms *via* a simple pathway. To date, only a few cases have been successful in the synthesis of ultrathin 2D metal[22] and metal oxide nanosheets[23,24] using graphene oxide (GO) as a template. Recently, our group used a GO paper as a template to obtain an ultralight single MO paper with tunable thickness and transparency.[25]

A graphene paper or film derived from various graphene-like materials such as GO, reduced graphene oxide (rGO) and pristine graphene has captured significant interest in a wide range of areas from physics,[26] materials science,[27] and chemistry[28] to environmental engineering.[29] In particular, the GO paper is widely used since it is prepared *via* assembling single-layer GO nanosheets, which are functionalized by abundant oxygen-containing groups and many defects on both their planes and

[a]*College of Life Science and Technology, Xinjiang University, Urumqi 130046, China. E-mail: zhang78089680@sina.com*

[b]*Department of Chemistry, Technical University of Denmark, DK-2800 Kongens Lyngby, Denmark. E-mail: cq@kemi.dtu.dk*

[c]*The State Key Laboratory for Modification of Chemical Fibers and Polymer Materials, College of Materials Science and Engineering, Donghua University, Shanghai 201620, China*

† Electronic supplementary information (ESI) available: Experimental detail, supporting microscopy images, XPS spectra and nitrogen adsorption–desorption isotherm. See DOI: 10.1039/c9ra08223a

edges. As a result, GO paper can capture ions and nanoparticles or covalently bind with other functional groups.[30] GO paper also displays a well-defined layer-by-layer porous nanostructure, with a d-spacing of about 1.2 nm, which allows ions to diffuse into the nanometer-scale pores of their interlayers.[31] Most importantly, GO paper can be easily decomposed and removed by application of high temperature in an oxygen-rich atmosphere. Consequently, GO paper is one of the most desirable sacrificial templates for the synthesis of layer-by-layer, nanoporous and ultrathin 2D metal or metal oxide nanosheets.

In this work, GO paper was prepared *via* the vacuum filtration of GO solution and was further used as a template for the synthesis of 2D CuO/ZnO/carbon paper on a large scale. Cu^{2+} and Zn^{2+} were loaded on the GO paper *via* electrostatic interaction and physical absorption between the oxygen groups and the desired cation. After removal of GO by heat, the metal oxide maintained the layer-by-layer, ultrathin and nanoporous structure. More interestingly, the as-prepared ZnO–CuO hybrid films displayed significantly improved performances as a non-enzymatic sensor for the detection of glucose.

GO nanosheets was synthesized *via* a modified Hummer's method according to our previous work.[32,33] Subsequently, some advanced techniques were applied to characterize the obtained GO, such as UV-vis spectroscopy (Fig. S1†), AFM (Fig. S2†) and XPS (Fig. S3A†). All the results indicate a significant amount of oxygen-containing groups is present on the GO sheet surface, which significantly increased the sites for attaching positively charged molecular groups and nanoparticles on the GO sheet. In our case, Cu^{2+} and Zn^{2+} were successfully attached on the GO paper *via* the direct immersion of GO paper into the ion source solution, which was confirmed by XPS analysis (Fig. S4†). In this process,[25] the metal ions were incorporated into the GO paper. After heat treatment, the obtained MO papers (as shown in the insert picture in Fig. 2, S5 and S6†) mimicked the GO paper structure and the sample colour changed to white, black and black, respectively for ZnO/carbon, CuO/carbon, and CuO/ZnO/carbon.

The as-synthesized MO films were examined first by powder X-ray diffraction (Fig. 1). In the XRD pattern of ZnO, the definite line broadening of the XRD peaks indicates that the prepared material consisted of particles in the nanoscale range. From the XRD patterns analysis, we determined the peak intensity, position and width, and full-width at half-maximum (FWHM). The diffraction peaks located at $2\theta = 31.7°$, $34.4°$, and $36.3°$ correspond to the (100), (002), and (101) planes, respectively, exhibiting the characteristic diffractions of a mixed-valence compound with a face-centred cubic structure (PDF #36-1451). The XRD pattern of CuO shows peaks at $2\theta = 35.4°$, $38.7°$, and $48.7°$, corresponding to the (002), (111), and (202) planes, respectively. All the diffraction peak can be readily indexed to the standard monoclinic phase (PDF #48-1548) without characteristic peaks assigned to possible impurities such as Cu_2O or $Cu(OH)_2$. In the case of CuO/ZnO, it displayed the diffraction peaks of both CuO and ZnO. It should be noted, in the XRD patterns of all the MO paper, the diffraction peck located at $2\theta = 19.8°$ is attributed to the undestroyed graphene. XPS was also used to confirm that the CuO/ZnO hybrid materials were

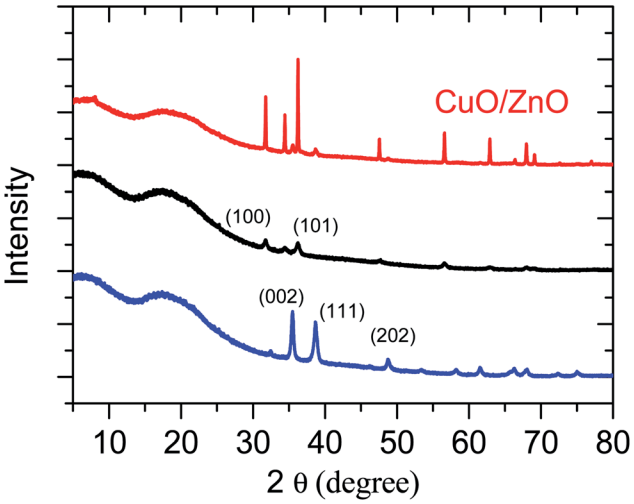

Fig. 1 XRD patterns of 2D nanoporous CuO/carbon, ZnO/carbon and hybrid CuO/ZnO/carbon papers.

obtained (see Fig. S5†). The binding energies of Cu $2p_{3/2}$, Zn $2p_{3/2}$, and O 1 s were identified at 933.63, 1021.9, and 529.67 eV, respectively. The high-resolution Cu and Zn scans indicate that both Cu and Zn were in the +2 oxidation state. The XPS measurements verify that the structures consist of CuO and ZnO, and furthermore, the atom ratio of Cu to Zn is about 1 : 1, suggesting that each cation has equal opportunity to diffuse in the interlayer GO paper. It should be mentioned that the carbon that appeared in Fig. S5A† comes from the undestroyed graphene paper template.

In general, MO is synthesized *via* chemical methods, where the shapes of most products are uncontrolled, and some further ligands are needed to prevent aggregation. Due to the fast grown process and no limit in growth direction, it is difficult to the control morphology of metal oxide. In our case, MO displayed ultrathin 2D nanosheets, with the size of about 20 nm and 50 nm corresponding to ZnO and CuO, respectively, according to TEM images shown in Fig. 2 and S6–S8.† More interestingly, the TEM images suggest that the MO nanosheets connected each other, resulting in the formation of a continuous nanoporous network structure (the porous size ranged from about 5 nm to 10 nm). There are probable two reasons for the assembled nanoporous structure, one is that the MO nanosheets connected each other during the growth process, and the other is GO has lots defects and pores, which affected the growth of the MO nanosheets. As we expected, the BET surface area of the as-obtained CuO/ZnO/carbon hybrid material was estimated to be 80 $m^2\ g^{-1}$ (Fig. S8†), which was contributed by both the porous CuO/ZnO and undestroyed graphene, and the average pore size of ~10 nm. The high-resolution TEM image of CuO/ZnO in Fig. S8† shows lattice fringes with an interplanar spacing of 0.25 nm and 0.28 nm corresponding to the CuO 002 lattice face and ZnO 100 lattice face, respectively. The selected area electron diffraction (SAED) pattern in the inset in Fig. 2C is in good agreement with the XRD pattern and illustrates the polycrystalline structure of CuO/

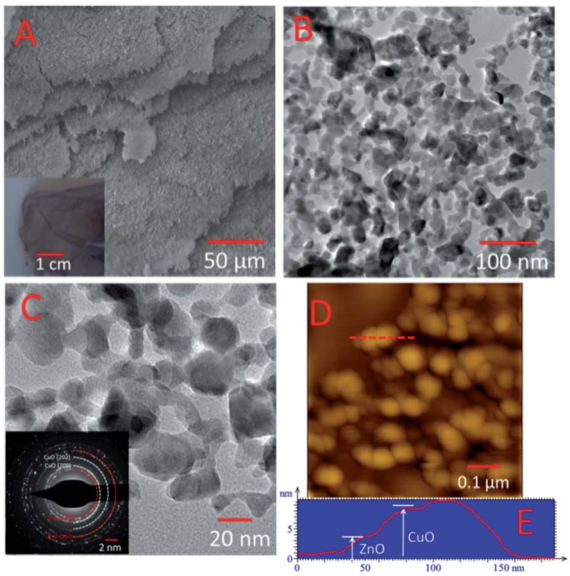

Fig. 2 SEM image of (A) CuO/ZnO/carbon and TEM images of (B and C) CuO/ZnO with different magnifications. The inset image of (A) is the picture of the CuO/ZnO/carbon paper, and the insert image of (C) is the diffraction pattern of the CuO/ZnO paper. (D) Detailed tapping mode AFM height images of CuO/ZnO and (E) line profile. The line profile was taken from the red lines marked in (D).

ZnO. The thickness of the nanosheets was measured *via* tapping mode AFM to be about 3 nm and 10 nm (Fig. 2D and S10†) for ZnO and CuO, respectively. Furthermore, from the SEM images (Fig. 2A and B) of CuO/ZnO, the layer-by-layer structure is clearly seen on the microscale, which is similar with our previous report.[25] Moreover, the density of the 2D nanoporous CuO/ZnO nanosheet was calculated to be about 50 mg cm^{-2}, which is 10 times lighter than commercial CuO nanoparticles.

To investigate the elemental of Cu and Zn distribution in the 2D nanoporous CuO/ZnO/carbon hybrid nanosheets, SEM and mapping analysis were performed for a single MO sheet. The SEM mapping images of the C, O, Cu and Zn elements are shown in Fig. 3. All the atoms were distributed uniformly in the nanocomposite, which suggests that a highly hybridized CuO/ZnO film was obtained. Both the high-resolution TEM image and FFT (Fig. S7C and D,† respectively) indicate that the single CuO and ZnO nanosheets connected with each other on the nanoscale, which will provide huge chances for the continuous formation of p–n junction interfaces on the nanoscale, which is beneficial for facile electron transfer.

More importantly, this type of layer-by-layer nanoporous CuO/ZnO/carbon nanosheet has a high surface area with conjunct bimodal pores, which can play key roles in providing shorter diffusion paths and rapid electrolyte transport, while providing more active sites for electrochemical reactions. The accurate detection of glucose is important for clinical diagnostics in diabetes control, analytical applications in biotechnology, and the food industry. Enzyme-based amperometric glucose biosensors can satisfy the requirements of clinical blood glucose level measurement. Glucose oxidase (GOx)-modified electrodes are the most common class of

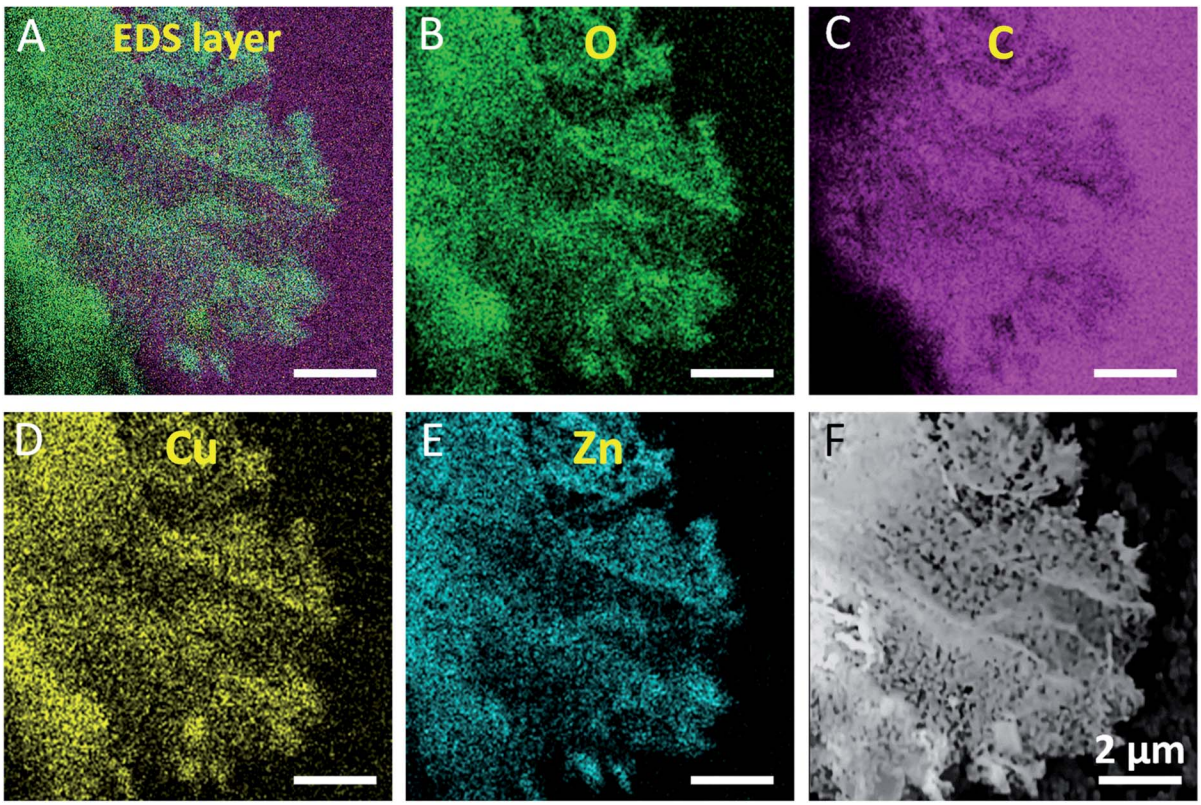

Fig. 3 EDX mapping images of a single 2D nanoporous CuO/ZnO/carbon nanosheet. (A) Superimposed EDS image, (B)–(E) images of the elemental distributions, and (F) corresponding TEM image. Scale bar: 2 μm.

amperometric biosensors for glucose detection because GOx enables the catalytic oxidation of glucose with high sensitivity and selectivity. However, enzyme-modified electrodes have some disadvantages. For instance, the instability of the electrode and unsatisfactory reproducibility, complicated immobilization procedures, and expensive enzymes are easily deactivated. Thus, to address these issues, the development of non-enzymatic sensors with high sensitivity and stability, and interference-free glucose determination is very important. According to the XRD and XPS results, graphene was not completely removed, and thus graphene could still exist as a film coated with metal oxide surface or edge, which will be beneficial for electron transfer. Accordingly, the 2D CuO/ZnO nanosheets may exhibit good electrochemical performances as non-enzymatic sensors for the detection of glucose.

Owing to their high specific area, 2D nanoporous nanosheets are promising materials for the fabrication of non-enzymatic glucose sensors. The cyclic voltammetry profiles of the 2D nanoporous CuO, ZnO and CuO/ZnO hybrid nanosheet-modified GCE electrodes in 40 mL 0.1 M KOH solution with and without 1 mM glucose were studied (Fig. 4). Obvious reduction peaks at around 0.6 V (*vs.* SCE) can be observed in the blank NaOH solution, which corresponds to the Cu(II)/Cu(III) redox couple according to previously reported studies (eqn (1)) (except the pure ZnO nanosheet electrode). After the injection of glucose, the Cu(III) ion obtains an electron and acts as an electron delivery system, and electrons are transferred from glucose to the electrode, which leads to an increase in the peak current, and the reaction process is demonstrated in eqn (2). Comparing the CV without and with 1 mM glucose, the oxidation current dramatically increased, and the results suggest a kinetic limitation in the reaction between the redox sites of the CuO and CuO/ZnO modified-electrodes and glucose. Initially, the reaction potential was as low as 0.3 V (*vs.* SCE).

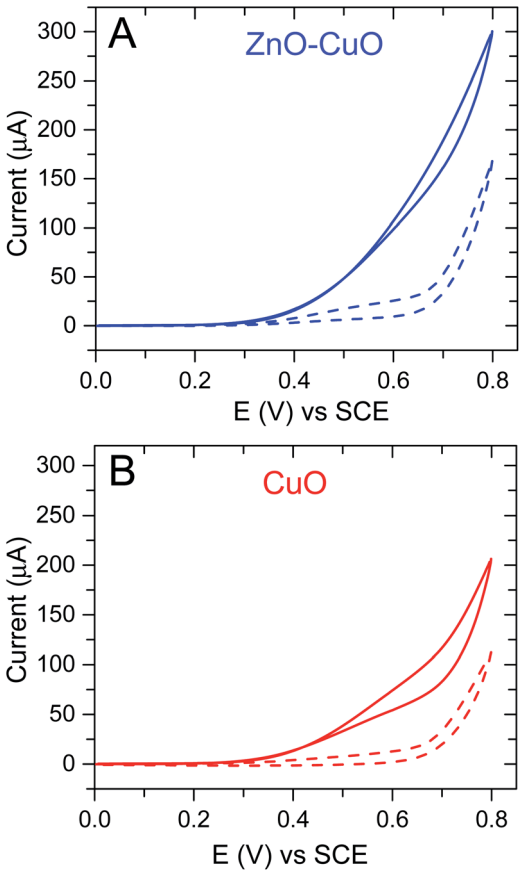

Fig. 4 CVs of the (A) ZnO–CuO/carbon and (B) CuO/carbon papers measured in 0.1 M KOH. The dashed line and solid line indicate the electrolyte without and with 1 mM glucose, respectively. Scan rate 50 mV s^{-1}.

$$CuO + OH^- \rightarrow CuO(OH) + e^- \quad (1)$$

$$CuO(OH) + \text{glucose} \rightarrow CuO + \text{gluconolactone} + H_2O \quad (2)$$

To evaluate the electrochemical performance for the analysis of glucose, the non-enzymatic amperometric detection of glucose was performed at 0.6 V (*vs.* SCE) with the successive addition of glucose. Fig. 5A and B show the *I–t* curves of the different 2D porous ZnO, CuO and CuO/ZnO nanosheet-modified GCE electrodes in 0.1 M NaOH solution upon the successive addition of different concentrations of glucose. Both CuO and CuO/ZnO showed the typical steady-step response with very low noise, and remarkable increase in the oxidation current, which show the electrocatalytic activity of the modified electrodes towards the oxide of glucose. A linear relationship between the glucose concentration and catalytic current was found in the range of 5 μM to 3.325 mM at the CuO/ZnO/carbon-modified electrode (Fig. 5C), with a detection limit of 0.5 μM. The linear regression equation with a high correlation coefficient (R) of 0.998 was obtained, and the sensitivity was estimated to be 3850 μA cm^{-2} mM^{-1}, which is over 3-fold higher than that for CuO (≈1000 μA cm^{-2} mM^{-1}). It is understood that the formation of a p–n junction in the CuO/ZnO heterostructures results in the extension of the space charge region, which locally narrows the conducting channel for the charge carriers in ZnO, thus making the p–n junction more sensitive to glucose-induced charge transfer. The application of CuO/ZnO as a glucose sensor involves two types of sensing behaviours: adsorption-induced surface depletion and chemical conversion with a change in the electrical potential. It is also notable that the active area of CuO increased in the heterostructures.

Since the 2D nanoporous CuO/ZnO acts as glucose oxidase, the electrochemical version of the Michaelis–Menten equation (eqn (3)) was used to evaluate the Michaelis constant (K_m).

$$j_{cat} = nFA\frac{k_{cat}S}{K_m + S} \quad (3)$$

where j_{cat} is the catalyst current obtained using the *I–t* curve, S is the glucose concentration, A is the surface area, n is number of electrons transferred, F is the Faraday constant, and K_{cat} is the apparent catalytic turnover rate. Considering n, F, A and K_{cat} as constants, eqn (3) could be simplified to eqn (4).

$$j_{cat} = \frac{KS}{K_m + S} \quad (4)$$

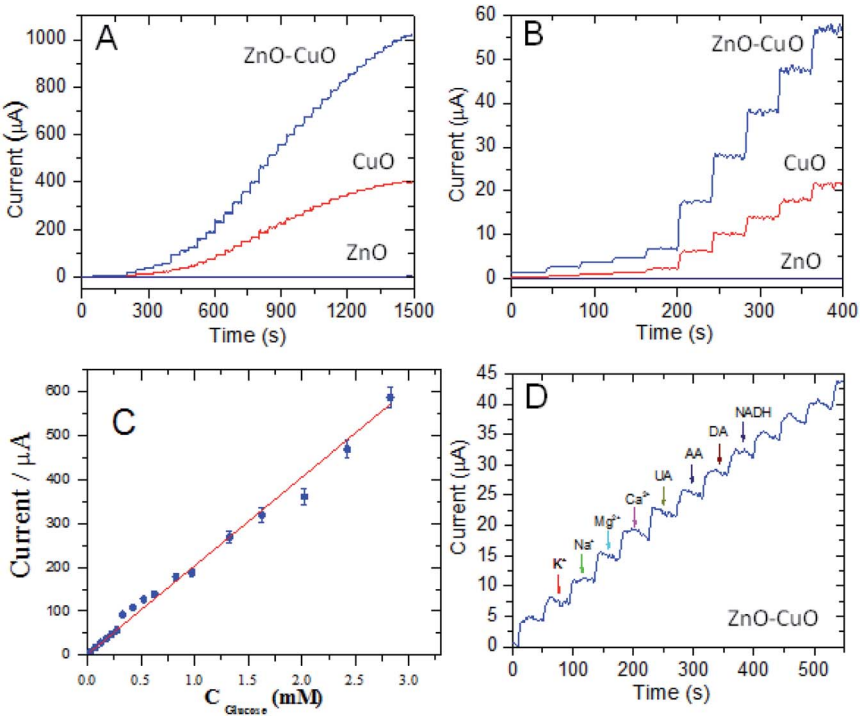

Fig. 5 Quantitative detection of glucose and selectivity analysis. (A) Full-range amperometric responses to the successive addition of glucose for three types of MO papers, (B) enlarged amperometric curves in the low-concentration region, (C) calibration curves, and (D) selectivity analysis by adding possible interfering species, while the successive addition of glucose was performed. Electrolyte 0.1 M KOH, and working electrode potential fixed at 0.6 V *vs.* (SCE).

As shown in Fig. S10,† the *I–t* curve could be fitted using eqn (4) with $R = 0.999$ and K_m is 5.4 mM. The apparent K_m is relatively low, close to that of a GOD-based sensor,[33] which suggests that the 2D CuO/ZnO/carbon displays good biocompatibility and has a high biological affinity to glucose.

To further verify its sensing performance, some electrochemical characteristic tests were performed on the 2D porous CuO/ZnO/carbon nanosheet-based electrode. First, the reproducibility of the 2D porous CuO/ZnO nanosheet for nonenzymatic glucose sensing was evaluated. Three modified electrodes were prepared, and the relative standard deviation (RSD) was no more than 8.7% for the current response, indicating satisfactory electrode-to-electrode reproducibility. Additionally, the recovery was 97% with an RSD of 3.5% (S/N = 3) for 25 μM of glucose, demonstrating good intra-electrode reproducibility. To explore the specific detection of glucose in a real sample using the proposed approach based on the 2D nanoporous CuO/ZnO nanosheet-modified electrode, the *I–t* curve of the 2D CuO/ZnO nanosheet-modified GCE electrode was measured in 0.1 M NaOH solution upon the successive

Table 1 Comparison of salivary glucose detection using various sensing electrodes

Detection method	Material	Sensitivity ($\mu A\ mM^{-1}\ cm^{-2}$)	LOD (mM)	Linear range (mM)	Reference
Electrochemical biosensors	CuO PN	2299	0.41×10^{-3}	0.005–0.825	34
	Ni–SnOx/PANI/CuO	1325	0.130	1–10	35
	CuO@C/D	1650	0.5×10^{-3}	0.5×10^{-3} to 4	36
	CuO-NPs	1098.37	0.59×10^{-3}	5×10^{-3} to 0.6	37
	CuO/GO/GCE	262.52	0.69×10^{-3}	2.79×10^{-3} to 2.03	38
	Nafion/GOx/ZnO/FcC11SH/Au	0.0278	—	0.05–1.0	39
	ZnO–CuO HNCs	3066.4	0.21×10^{-3}	0.47×10^{-3} to 1.6	19
	CuO–ZnO NRs/FTO	2961.8	0.4×10^{-3}	0.001–8.45	40
	ZnO–CuO core–shell spheres	1217.4	1.677×10^{-3}	0.02–4.86	13
Plasmon-aided biosensors	Half-rough Au/NiAu MNAs	483	1×10^{-3}	0.005–31	41
Photoelectrochemical sensor	Au–NiO_{1-x} HNAs	1777	1×10^{-3}	0.005–7	42
Photoelectrochemical sensor	$BiVO_4$	—	0.13×10^{-3}	0–5	43
Electrochemical sensors	Hybrid CuO/ZnO/carbon papers	3850	0.5×10^{-3}	5×10^{-3} to 3.325	This work

addition of 25 μM of glucose. Furthermore, the electrochemical response of common interfering species for 2D porous CuO/ZnO nanosheet-modified GCE electrode was examined, as shown in Fig. 5D. Some common interfering species in human serum, such as 250 μM uric acid (UA), ascorbic acid (AA), dopamine acid (DA), nicotinamide adenine dinucleotide (NADH), Mg^{2+}, K^{+}, Na^{+} and Ca^{2+}, were chosen as the interfering species. As is clearly seen in Fig. 5D, the current responses of the interfering species has little effect compared to glucose, which indicated that 10 times higher concentration of interfering species than glucose has no response for the detection 25 μM glucose. Here, the good selectivity of the 2D nanoporous CuO/ZnO nanosheet against some reducing compounds, such as AA, can be ascribed to the obvious repulsion with the negatively charged CuO and ZnO (the isoelectric point of both is about 9.5) and the negatively charged AA (deprotonated) under highly basic conditions. The good selectivity of the 2D porous CuO/ZnO/carbon nanosheet electrode for glucose and against other interfering materials can be ascribed to the synergetic action of the well-designed 2D porous structure and high surface area, which provides the maximum number of active free paths to the glucose molecules and facilitates faster electron transfer. The results obtained with the proposed method were compared with other methods for the detection of glucose (Table 1). Compared with other structures of CuO or CuO/ZnO, the as-prepared 2D nanoporous CuO/ZnO/carbon has good reliability and can be used in the actual detection of glucose.

Conclusions

Herein, 2D CuO/ZnO heterostructures were successfully synthesized using GO paper as a sacrificial template, which displayed a highly porous and layer-by-layer structure. This method can be expanded to prepare 2D porous metal oxide nanosheets for application as non-enzymatic sensors for the detection of glucose, photocatalytic degradation organic pollution and energy conversion and storage.

Conflicts of interest

There are no conflicts to declare.

Acknowledgements

This work was supported by the Danish Research Council for Technology and Product Science (Project No. 12-127447). M. Z. acknowledges National Natural Science Foundation of China (No. 31960496), National Natural Science Foundation of Xinjiang (No. 2018D01C040) and the research start-up fund of Xinjiang University. C. H. is grateful for the Ørsted-Marie Curie Cofunded postdoc fellowship, DHU Distinguished Young Professor Program (LZB2019002), and Young Elite Scientists Sponsorship Program by CAST (2017QNRC001).

References

1 S. Daemi, S. Ghasemi and A. A. Ashkarran, *J. Colloid Interface Sci.*, 2019, **550**, 180–189.
2 S. Hwang, Y. Kim, S. Hong and S. Lim, *Sensors*, 2019, **19**, 3151.
3 J. Kim, W. Kim and K. Yong, *J. Phys. Chem. C*, 2012, **116**, 15682–15691.
4 L. Wang, Y. Kang, Y. Wang, B. Zhu, S. Zhang, W. Huang and S. Wang, *Mater. Sci. Eng., C*, 2012, **32**, 2079–2085.
5 C. Wang, J. Zhu, S. Liang, H. Bi, Q. Han, X. Liu and X. Wang, *J. Mater. Chem. A*, 2014, **2**, 18635–18643.
6 M. T. Qamar, M. Aslam, I. M. I. Ismail, N. Salah and A. Hameed, *ACS Appl. Mater. Interfaces*, 2015, **7**, 8757–8769.
7 C. Karunakaran, R. Dhanalakshmi, P. Gomathisankar and G. Manikandan, *J. Hazard. Mater.*, 2010, **176**, 799–806.
8 J. Sun, G. Yang, Y. Yoneyama and N. Tsubaki, *ACS Catal.*, 2014, **4**, 3346–3356.
9 A. Kargar, Y. Jing, S. J. Kim, C. T. Riley, X. Pan and D. Wang, *ACS Nano*, 2013, 11112–11120.
10 B. S. Kang, S. E. Ahn, M. J. Lee, G. Stefanovich, K. H. Kim, W. X. Xianyu, C. B. Lee, Y. Park, I. G. Back and B. H. Park, *Adv. Mater.*, 2008, **20**, 3066–3069.
11 A. Ghosh, B. B. Show, S. Ghosh, N. Mukherjee, G. Bhattacharya, S. K. Datta and A. Mondal, *RSC Adv.*, 2014, **4**, 51569–51575.
12 C. Wang, J. Zhu, S. Liang, H. Bi, Q. Han and X. Liu, *J. Mater. Chem. A*, 2014, **2**, 18635–18643.
13 B. Cai, Y. Zhou and M. Zhao, *Appl. Phys. A: Mater. Sci. Process.*, 2015, **118**, 989–996.
14 B. Li and Y. Wang, *Superlattices Microstruct.*, 2010, **47**, 615–623.
15 A. Zainelabdin, G. Amin, S. Zaman, O. Nur, J. Lu, L. Hultman and M. Willander, *J. Mater. Chem.*, 2012, **22**, 11583–11590.
16 K. Ghanbari and N. Hajheidari, *Anal. Biochem.*, 2015, **473**, 53–62.
17 R. D. Corpuz and J. R. Albia, *Mater. Res.*, 2014, **17**, 851–856.
18 M. M. Günter, T. Ressler, B. Bems, C. Büscher, T. Genger, O. Hinrichsen, M. Muhler and R. Schlögl, *Catal. Lett.*, 2001, **71**, 37–44.
19 C. Zhou, L. Xu, J. Song, R. Xing, S. Xu, D. Liu and H. Song, *Sci. Rep.*, 2014, **4**, 7382.
20 S. Jung and K. Yong, *Chem. Commun.*, 2011, **47**, 2643–2645.
21 Z. Sun, T. Liao, Y. Dou, S. M. Hwang, M.-S. Park, L. Jiang, J. H. Kim and S. X. Dou, *Nat. Commun.*, 2014, **5**, 3813.
22 Z. Lu, J. Zhu, D. Sim, W. Zhou, W. Shi, H. H. Hng and Q. Yan, *Chem. Mater.*, 2011, **23**, 5293–5295.
23 H. Cao, X. Zhou, C. Zheng and Z. Liu, *ACS Appl. Mater. Interfaces*, 2015, **7**, 11984–11990.
24 Z. Huang, A. Zhou, J. Wu, Y. Chen, X. Lan, H. Bai and L. Li, *Adv. Mater.*, 2016, **28**, 1703–1708.
25 M. Zhang, C. Hou, A. Halder and Q. Chi, *ACS Appl. Mater. Interfaces*, 2017, **9**, 3922–3930.
26 G. Liu, W. Jin and N. Xu, *Chem. Soc. Rev.*, 2015, **44**, 5016–5030.

27 Y. Shao, M. F. El-Kady, L. J. Wang, Q. Zhang, Y. Li, H. Wang, M. F. Mousavi and R. B. Kaner, *Chem. Soc. Rev.*, 2015, **44**, 3639–3665.
28 H. Cong, J. Chen and S. Yu, *Chem. Soc. Rev.*, 2014, **43**, 7295–7325.
29 M. Zhang, C. Hou, A. Halder, H. Wang and Q. Chi, *Mater. Chem. Front.*, 2017, **1**, 37–60.
30 B. Mi, *Science*, 2014, **343**, 740–742.
31 M. Zhang, A. Halder, C. Hou, J. Ulstrup and Q. Chi, *Bioelectrochemistry*, 2016, **109**, 87–94.
32 M. Zhang, C. Hou, A. Halder, J. Ulstrup and Q. Chi, *Biosens. Bioelectron.*, 2017, **89**, 570–577.
33 A. Halder, M. Zhang and Q. Chi, *Biosens. Bioelectron.*, 2017, **89**, 570–577.
34 P. Chakraborty, S. Dhar, N. Deka, K. Debnath and S. P. Mondal, *Sens. Actuators, B*, 2019, **302**, 127–134.
35 A. Sedighi, M. Montazer and S. Mazinani, *Biosens. Bioelectron.*, 2019, **135**, 192–199.
36 Z. Zhai, B. Leng, N. Yang, B. Yang, L. Liu, N. Huang and X. Jiang, *Small*, 2019, **9**, 1–11.
37 Q. Wu, L. He, Z. Jiang, Y. Li, Z. Cao, C. Huang and Y. Li, *Biosens. Bioelectron.*, 2019, **145**, 111704.
38 J. Song, L. Xu, C. Zhou, R. Xing, Q. Dai, D. Liu and H. Song, *ACS Appl. Mater. Interfaces*, 2013, **5**, 12928–12934.
39 Q. Ma and K. Nakazato, *Biosens. Bioelectron.*, 2014, **51**, 362–365.
40 R. Ahmad, N. Tripathy, M. Ahn, K. Bhat, T. Mahmoudi, Y. Wang, J. Yoo, D. Kwon, H. Yang and Y. B. Hahn, *Sci. Rep.*, 2017, **7**, 1–10.
41 L. Wang, W. Zhu, W. Lu, X. Qin and X. Xu, *Biosens. Bioelectron.*, 2018, **111**, 41–46.
42 W. Meng, Y. Wen, L. Dai, Z. He and L. Wang, *Sens. Actuators, B*, 2018, **260**, 852–860.
43 S. Wang, S. Li, W. Wang, M. Zhao, J. Liu, H. Feng, Y. Chen, Q. Gu, Y. Du and W. Hao, *Sens. Actuators, B*, 2019, **291**, 34–41.

